The Astrophysical Journal Letters, 847:L11 (7pp), 2017 September 20 https://doi.org/10.3847/2041-8213/aa8acd

Probing Large-scale Coherence between *Spitzer* IR and *Chandra* X-Ray Source-subtracted Cosmic Backgrounds

N. Cappelluti[1,2], R. Arendt[3,4], A. Kashlinsky[4,5], Y. Li[6], G. Hasinger[6], K. Helgason[7], M. Urry[1,2], P. Natarajan[8], and A. Finoguenov[9,10]

[1] Yale Center for Astronomy and Astrophysics, P.O. Box 208120, New Haven, CT 06520, USA
[2] Department of Physics, Yale University, P.O. Box 208120, New Haven, CT 06520, USA
[3] University of Maryland, Baltimore County, 1000 Hilltop Circle, Baltimore, MD 21250, USA
[4] Observational Cosmology Laboratory, NASA Goddard Space Flight Center, Code 665, Greenbelt, MD 20771, USA
[5] SSAI, 10210 Greenbelt Road, Suite 600, Lanham, MD 20706, USA
[6] Institute for Astronomy, University of Hawaii, 2680 Woodlawn Drive, Honolulu, HI 96822, USA
[7] Department of Astronomy, Yale University, P.O. Box 208101, New Haven, CT 06520, USA
[8] Max Planck Institute for Astrophysics, Karl-Schwarzschild-Str. 1, D-85748 Garching, Germany
[9] Max-Planck-Institut für extraterrestrische Physik, Postfach 1312, D-85741, Garching bei München, Germany
[10] Department of Physics, University of Helsinki, Gustaf Hällströmin katu 2a, FI-00014 Helsinki, Finland
Received 2017 July 11; revised 2017 August 29; accepted 2017 September 6; published 2017 September 21

Abstract

We present new measurements of the large-scale clustering component of the cross-power spectra of the source-subtracted *Spitzer*-IRAC cosmic infrared background and *Chandra*-ACIS cosmic X-ray background surface brightness fluctuations Our investigation uses data from the *Chandra* Deep Field South, *Hubble* Deep Field North, Extended Groth Strip/AEGIS field, and UDS/SXDF surveys, comprising 1160 *Spitzer* hours and ∼12 Ms of *Chandra* data collected over a total area of 0.3 deg^2. We report the first ($>5\sigma$) detection of a cross-power signal on large angular scales $>20''$ between [0.5–2] keV and the 3.6 and 4.5 μm bands, at $\sim5\sigma$ and 6.3σ significance, respectively. The correlation with harder X-ray bands is marginally significant. Comparing the new observations with existing models for the contribution of the known unmasked source population at $z < 7$, we find an excess of about an order of magnitude at 5σ confidence. We discuss possible interpretations for the origin of this excess in terms of the contribution from accreting early black holes (BHs), including both direct collapse BHs and primordial BHs, as well as from scattering in the interstellar medium and intra-halo light.

Key words: cosmology: observations – diffuse radiation – infrared: diffuse background – quasars: supermassive black holes – X-rays: diffuse background

1. Introduction

The cosmic infrared background (CIB) is produced from the integrated radiation resulting from stars, accretion, and dust reprocessing, from the epoch of the last scattering to the present. Although most of the CIB flux has been resolved into discrete sources, a sizable fraction of them are inaccessible for telescopic follow-up studies either because they are intrinsically faint or very distant. Of particular interest is the study of the contribution to the CIB from sources at the epoch of the first stars and black holes (BHs). Current understanding of structure formation suggests that these first UV-bright objects form between $z = 15$–25, and their radiation would be redshifted to the infrared today. Therefore, the properties of the CIB—in particular, the surface brightness fluctuations—offer a new window to access these high-redshift sources by studying the residuals after the removal of known sources.

An excess, of about a factor >20, on scales larger than $\sim30''$ with respect to known, $z < 6$, populations was detected by Kashlinsky et al. (2005, 2007b, 2012), and confirmed by Cooray et al. (2012b) with *Spitzer* after removing sources to $m_{AB} = 24$–25 at 3.6 μm and 4.5 μm, and Matsumoto et al. (2011) and Seo et al. (2015) with *AKARI* below $m_{AB} = 23$–24 at 2.4, 3.2, and 4.1 μm. Its origin is debated: it can be attributed entirely to high-redshift sources (Kashlinsky et al. 2007b, 2012; Yue et al. 2013) or to diffuse intra-halo light around galaxies at $z = 1$–5 (Cooray et al. 2012a; Zemcov et al. 2014) and (Kashlinsky 2017 for a review). At shorter wavelengths, not directly relevant to this study, the situation is less clear with conflicting measurements from 2MASS (Kashlinsky et al. 2002; Odenwald et al. 2003), NICMOS (Thompson et al. 2007a, 2007b), and CIBER (Zemcov et al. 2014) as discussed in detail in Section 2.1.2 of Kashlinsky et al. (2015).

Cappelluti et al. (2013) measured a statistically significant cross-power spectrum between the source-subtracted *Spitzer* CIB and *Chandra* cosmic X-ray background (CXB) [0.5–2] keV fluctuations in the Extended Groth Strip (EGS), suggesting that sources responsible for the CIB excess share the same environment with, or are, accreting BHs. This result was confirmed by Mitchell-Wynne et al. (2016). Neither study was able to probe with high significance the cross-power at the largest scales (i.e., $>20''$–$30''$) arising from clustering. Helgason et al. (2014) showed that known source populations alone (X-ray binaries, AGNs, and hot gas) are not sufficient to account for the tentative large-scale component seen in the cross-power. Yue et al. (2013) interpreted this excess CIB power and the CIB–CXB coherence as arising from a population of direct collapse black holes (DCBH; see, e.g., Lodato & Natarajan 2006, 2007 and references therein) at $z > 12$. Alternatively, Kashlinsky (2016) suggested that the measured CIB fluctuations could be explained naturally if LIGO events arise from primordial BHs (of ∼20–40 $M_\odot$) making up the dark matter (Bird et al. 2016),

Here, we present the first measurement of the clustering component in the source-subtracted CIB versus CXB fluctuation cross-power spectra, between four photometric band pairs,

Table 1
X-Ray Map Properties

Field	FoV (arcmin)	Pixel Scale (arcsec)	$\sum$Exp (Ms)	$\langle$Exp$\rangle$ (Ms)	$N_{\rm ph,tot0.5-2}$	$N_{\rm ph,Astr.(0.5-2)}$	$N_{\rm ph,tot(2-7)}$	$N_{\rm ph,Astr.(2-7)}$	$\%_{\rm mask}$	Catalog
HDFN	$9\farcm6 \times 5\farcm1$	$0\farcs6$	1.79	1.62	91904	55956	187911	99693	38%	Alexander et al. (2003)
CDFS	$12\farcm6 \times 9\farcm5$	$0\farcs6$	6.67	5.96	760651	110698	1943340	130973	40%	Luo et al. (2017)
EGS	$45\farcm2 \times 9\farcm5$	$1\farcs2$	2.25	0.75	89484	49832	232297	118227	32%	Goulding et al. (2012)
UDS	$20\farcm4 \times 20\farcm4$	$1\farcs2$	1.19	0.43	59995	28792	134819	66700	36%	D. Kocevski et al. (2017, in preparation)

by combining the deepest *Spitzer* and *Chandra* observations available to date.

2. Data Sets and Map Production

2.1. Chandra *X-Ray data*

The X-ray data are from the deep *Chandra* ACIS-I AEGIS survey (EGS; Goulding et al. 2012; Nandra et al. 2015), the UDS-SXDF field (D. Kocevski et al. 2017, in preparation), the *Chandra* Deep Field South (CDFS; Luo et al. 2017), and the Hubble Deep Field North (HDFN; Alexander et al. 2003). In total, we used 243 *Chandra* pointings yielding a total of 11.9 Ms of flare-cleaned data, over an area of 0.3 $\deg^2$ (see Table 1). The data analysis methods used have been described in detail in Cappelluti et al. (2013) and Mitchell-Wynne et al. (2016), except that here we apply a stricter rejection of flares (see Cappelluti et al. 2017) and use both the FAINT and VFAINT telemetry mode data.

We created count maps in the [0.5–2] keV and [2–7] keV energy bands from even (A) and odd (B) events to evaluate the noise floor for the cross-power (see below). We produced X-ray masks, M_X, with the catalogs listed in Table 1, by cutting circular regions of $7''$ radius around each point source: this removes >90% of known X-ray source fluxes over the field.

We masked all the extended emission identified with groups and clusters of galaxies. Sensitivities and redshift ranges vary slightly from field to field and are discussed in Finoguenov et al. (2015), Erfanianfar et al. (2013), Finoguenov et al. (2010), and Erfanianfar et al. (2014) for CDFS, EGS, UDS, and HDFN, respectively (see Figure 3).

Multiplying M_X by the corresponding IR masks, $M_{\rm IR}$, we obtain $M_{{\rm IR},X}$ (Kashlinsky et al. 2007b, 2012; Cappelluti et al. 2013; and see below). In Table 1, we summarize the number of X-ray counts in the maps after masking. The background was modeled with two components, one from particles/instrument and one from astrophysical sources. The first component, X_p, has been estimated with the ACIS-*stowed* event files (e.g., Hickox & Markevitch 2006; Cappelluti et al. 2013, 2017) and the second, $X_{\rm Cosm}$, by distributing remaining counts in the field according to an exposure map, E (for an extensive discussion see Cappelluti et al. 2013, 2017); the mean X-ray map is $\langle X\rangle = (X_p + X_{\rm Cosm}) * M_{{\rm IR},X}$. The fluctuation map is then given as $\delta F^i_{X_{\rm raw}} = X^i/E^i - \langle X^i\rangle/E^i$, where X^i are the X-ray counts at the position i. We weighted our maps to take vignetting into account and the resulting fluctuation map is $\delta F^i_X = \delta F^i_{X_{\rm raw}} * E^i/\langle E\rangle$.

2.2. Spitzer *IR Data*

The *Spitzer*/IRAC self-calibrated mosaics are the same data (program ID = 169, 194, 61041, 61042) that were analyzed in Kashlinsky et al. (2007a, 2012) and described in detail in Arendt et al. (2011). We have reprocessed the observations with a new version of the self-calibration. Both epochs of the observations for each field were self-calibrated simultaneously using a new data model. The single field of view "ultra-deep" portion of the HDFN was still omitted, as well as the southern part of the HDFN, which was affected by an artifact. The new data model can be written as $D^i = S^\alpha + F^{p,r} + F^q$, where D^i are the data in the ith pixel, S^α is the sky intensity at position α, $F^{p,r}$ is the "fixed" detector offset for each pixel p for each group of frames (AOR) r, and F^q is the "variable" detector offset as a function of frame and output q (cf. Arendt et al. 2011).

The new feature included in our analysis is the addition of the r index, which allows the fixed detector offset to vary in time. Previously, the data from each AOR were self-calibrated separately to derive the F^p terms individually, and then the results were merged and remapped. Because of the changing zodiacal light between epochs, we had not been able to combine the observations. With the new self-calibration model, consistency of the derived sky and the $F^{p,r}$ and F^q offsets is now built into the procedure. The resulting sky maps do not exhibit large-scale variations caused by combining epochs. In addition, our enhanced procedure also slightly reduces small-scale variations (noise) because the offsets are being determined relative to a sky that is the average of all the available data, not just the data from 1 AOR. All maps were then clipped to the same shot noise level $P_{\rm SN} = 50$ and $P_{\rm SN} = 30\,{\rm nJy\,nW\,m^{-2}\,sr^{-1}}$ in 3.6 μm and 4.5 μm, respectively, or down to $m_{AB} \sim 24.8$ mag. X-ray maps astrometry has been matched to that of the IR maps with pixel scales of $0\farcs6$ for HDFN and CDFS and $1\farcs2$ for the UDS and EGS.

3. Fluctuation Analysis

After masking detected-source pixels, we study the surface brightness fluctuation field, δF, and compute its Fourier transform $\Delta(q)$ using a fast Fourier transform with q as the angular frequency. The power spectrum in a single band n is $P_n(q) = \langle|\Delta(q)|^2\rangle$, where the average is taken over the interval $[q, q + dq]$ and its error is $\sigma_{P_n}(q) = P_n(q)/\sqrt{N_q}$, where N_q is the number of independent Fourier elements adopted in the analysis, and $\sqrt{q^2 P_n(q)/2\pi}$ is the typical rms fluctuation in the flux on a scale with wavelength $2\pi/q$. In this study, the masked pixels occupy 30%–40% of the maps (see Table 1), which allows for a robust FFT analysis (Kashlinsky et al. 2012). In order to determine the intensity and structure of the joint fluctuations for every pair of independent photometric bands, we estimated the cross-power spectrum using $P_{m,n}(q) = \Delta_m(q)\,\Delta_n(q)^* = {\rm Re}_m(q)\,{\rm Re}_n(q) + {\rm Im}_m(q){\rm Im}_n(q)$, where Re and Im refer to the real and imaginary parts of the Fourier transform.

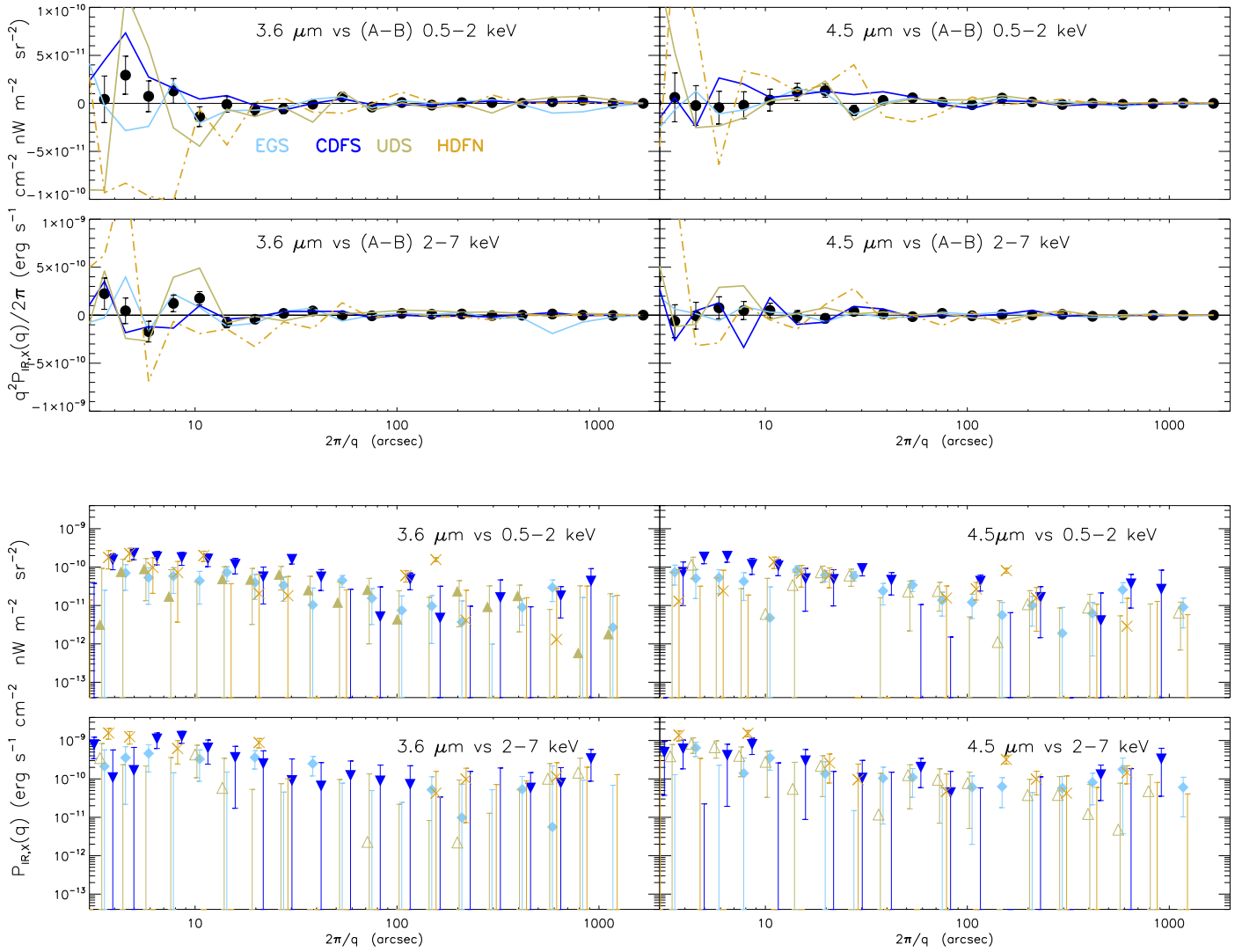

Figure 1. Top panels: the mean square fluctuation cross-power spectra between CIB fluctuations and CXB (A–B) maps as a function of the angular scale; these indicate the level of systematic error in our analysis. From top left to bottom right: 3.6 μm vs. 0.5–2 keV, 4.5 μm vs. 0.5–2 keV, 3.6 μm vs. 2–7 keV, and 4.5 μm vs. 2–7 keV, respectively. The noise is roughly 10 times lower for the soft X-ray band (top panels) compared to the hard X-ray band (next two panels). Colors refer to individual survey fields: cyan for EGS, blue for CDFS, light brown for UDS, and light orange for HDFN. The black filled circles show the combined cross-power for all four fields. Bottom panels: the same as the top panels, but between CIB and CXB fluctuation maps in individual fields. Order is the same as in the top panels. Cyan diamonds are EGS, blue inverted triangles are CDFS, light brown triangles are UDS, and light orange crosses are HDFN.

The errors are

$$\sigma_{P_{m,n}}(q) = \sqrt{P_m(q)P_n(q)/N_q}. \quad (1)$$

All of the IR maps have been clipped at the same shot noise level to combine the four fields to reduce cosmic and sample variance. We performed Fourier analysis in the four fields listed in Table 1 and averaged the cross-power spectra by weighting with their errors. In order to combine signals, all the fields of different geometries were binned in Fourier space to give power at identical q. The stacked cross-power is computed by averaging $\langle \Delta_m \Delta_n^* \rangle$ and its variance: $\sigma^2_{P_{(n,m)}}(q) = \frac{1}{\sum_{i=1}^{4}(\sigma^i_{P_{m,n}}(q))^{-2}}$.

3.1. Systematic Effects

One concern is the possibility of either random or spurious cross-correlation in the data. In order to evaluate this, we cross-correlated the IR fluctuations with the X-ray noise maps obtained by subtracting maps of even events (A) from maps of odd events (B). These A–B maps contain only random noise/artifacts (see Cappelluti et al. 2013). Figure 1 shows that this cross-power is very low at scales larger than ∼20 arcsec for every individual field and the combined fields; the larger deviations below 20 arcsec likely occur because the masked regions have these dimensions. The noise floor is about 1 dex higher for correlations with the hard X-ray band compared to the soft X-ray band, due to worse statistics. We conclude that in our maps noise and instrumental effects are uncorrelated on scales above an arcminute.

4. Results

For each survey field we evaluated the cross-power spectrum in four possible IR and X-ray band pairs, as shown in the lower panels of Figure 1. While in the individual fields there appears, at scales >20″, a significantly positive signal (Table 2) when cross-correlating CIB with [0.5–2] keV, its significance improves dramatically when we combine all four fields, as shown in Figure 2.

Table 2
Cross-power-spectrum Amplitude on $>20''$ in Units of 10^{-19} erg s^{-1} cm^{-2} nW m^{-2} sr^{-2}

	$2\pi/q > 20''$			
Field	3.6 μm vs. [0.5–2]	4.5 μm vs. [0.5–2]	3.6 μm vs. [2–7]	4.5 μm vs. [2–7]
HDFN	2.45 ± 2.16	0.05 ± 1.54	-18.62 ± 13.40	-6.64 ± 10.3
CDFS	3.41 ± 1.00	2.13 ± 0.85	9.00 ± 6.91	-0.38 ± 6.47
EGS	1.53 ± 0.46	1.98 ± 0.39	2.56 ± 3.79	4.77 ± 3.21
UDS	2.04 ± 0.94	1.57 ± 0.61	-7.50 ± 5.87	2.04 ± 3.35
STACK	1.87 ± 0.37	1.91 ± 0.34	2.73 ± 3.22	3.00 ± 2.76

On the angular scales sampled here, the correlations of 3.6 μm versus 0.5–2 keV, 4.5 μm versus 0.5–2 keV, and 4.5 μm versus 2–7 keV show a positive cross-power at the 6σ, 7.8σ, and 2.1σ confidence levels, respectively; for 3.6 μm versus [2–7] keV the signal is positive but consistent with zero at 1σ (cf. Mitchell-Wynne et al. 2016). The novelty of our analysis lies in the combination of deeper fields, at both IR and X-ray wavelengths, over a much larger area. The cross-power amplitude for the four combined fields on large scales ($20''$–$1500''$), reported in Table 2, is significant at 5σ and 6.3σ for 3.6 μm versus 0.5–2 keV and 4.5 μm versus 0.5–2 keV, respectively; there is no significant cross-power between either IR channel and the hard band X-rays. In the bottom panel of Figure 2, the broad 3.6+4.5 μm versus 0.5–2 keV and 2–7 keV cross-powers were obtained by averaging the measurements of P(q) in the sub-bands. At $5''$–$1500''$, the CIB correlates with the soft band at $>10\sigma$ and with the hard band at $\sim 3.5\sigma$. The correlation above $20''$ is significant at the $>10\sigma$ and 2.5σ level, for soft and hard X-ray bands, respectively.

As a reference, in order to evaluate the level of correlation between the two band pairs, we evaluated the level of coherence of the fluctuations $\mathcal{C} \sim 0.14$–0.20 for either IR channel versus the soft band.

5. Discussion

The significant cross-correlation signal arises from a population of sources that emit both in IR and X-rays or share the same environment. Known sources of extragalactic X-rays include (i) normal galaxies, (ii) AGNs, and (iii) hot gas in clusters and groups. In the following, we use the cross-power reconstruction of Helgason et al. (2014) with some improvements.

Galaxies contain high- and low-mass X-ray binaries whose X-ray luminosities scale with star formation rate and stellar mass, respectively (e.g., Basu-Zych et al. 2013):

$$L_{\rm X} = \alpha {\rm SFR}(1+z)^{\gamma} + \beta M_{\star}(1+z)^{\delta}\,, \quad (2)$$

where α, β, γ, and δ are parameters for which we adopt the values measured by Lehmer et al. (2016) in both the soft and hard bands and we include the intrinsic scatter in the relation. For the underlying galaxy population we use a semi-analytic galaxy formation model based on the Millennium simulation (Henriques et al. 2015), which is in good agreement with the observed star formation history and stellar mass function as a function of redshift.

We use the IR brightness and a projected position given by the model light cones to create a model image. The brightness distribution is also in a good agreement with observed galaxy counts and luminosity functions. We assign an X-ray brightness according to Equation (2) to the same image position based on the physical properties and the luminosity distance of the galaxy. To mimic the source masking, we eliminate all sources with an IR magnitude brighter than $m_{AB} = 24.8$ and calculate the angular power spectrum of the remaining sources in the same way as described in Section 3. The magnitude limit is tuned to match the shot noise level in the IR autopower spectrum, which is known to be galaxy-dominated. On large scales, however, the IR autopower spectrum is lower than measurements and is in agreement with Helgason et al. (2012).

For the AGN contribution, we adopt the population model of Gilli et al. (2007) in X-rays and Helgason et al. (2014) in the IR. The extent to which AGNs are removed by the joint IR/X-ray mask is estimated using empirical X-ray-to-optical relations (Civano et al. 2012; for details see Helgason et al. 2014). The fraction of removed sources as a function of brightness, referred to as the selection function, is shown in Figure 3. The extended tail of the AGN selection is due to the large intrinsic scatter in the X-ray to IR relation for AGNs and is the most uncertain factor in our calculation. The shot noise, however, gives us a constraint on how large this scatter can actually be. Interestingly, in order to simultaneously match the amplitude of the small-scale cross-power in the 0.5–2 keV and 2–7 keV bands we need to assume an extremely hard spectral slope ($\Gamma = 0.5$), possibly implicating heavily obscured AGNs responsible for the power on small scales.

Hot X-ray emitting gas in groups and clusters of galaxies spatially correlates with IR emitting sources sharing the same environments. We adopt the hot gas modeling of Helgason et al. (2014, Section 5.1.3), which uses the mass and extent of hot gas from the same semi-analytic model used for galaxies above (Guo et al. 2011; Henriques et al. 2015). We assume a beta-model density profile of hot gas in halos emitting with a simple Brehmmstrahlung spectrum determined by the gas temperature. Finally, we tune the average gas mass in halos (by a factor of 0.35) to match observed X-ray group/cluster counts (see Figure 3). To mimic the masking of groups in our several fields we adopt the 50% group detection completeness level of the ECDF-S (Finoguenov et al. 2015).

Figure 2 shows the contribution from galaxies, AGNs, and clusters to the cross-power of the unresolved IR and X-ray sources. All modeled cross-power spectra are multiplied by the *Chandra* beam for which we use the analytic profile given in Kolodzig et al. (2017). The evolution of the CXB production rate of the reconstructed populations is shown in Figure 3. The soft band X-ray flux expected from summing known but unresolved populations (Figure 3) is $\sim 2.6 \times 10^{-13}$ erg cm^{-2} s^{-1} deg^{-2}, which is $\sim 30\%$ of the still unresolved CXB flux or 2.5% of the total CXB flux (Cappelluti et al. 2017), so unknown population(s) contribute $\lesssim 7 \times 10^{-13}$ erg cm^{-2} s^{-1} deg^{-2}.

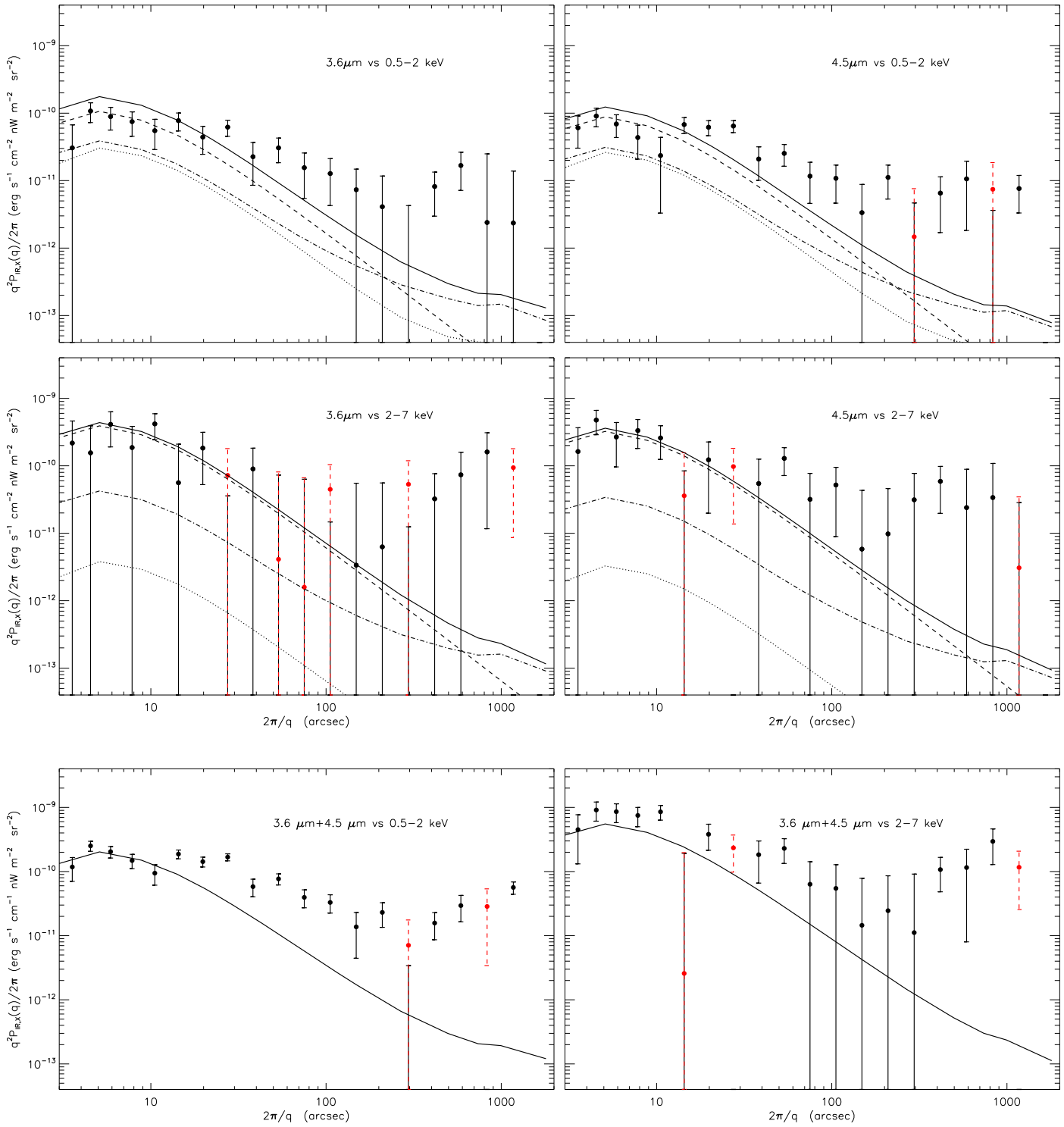

Figure 2. Combined CIB–CXB cross-power spectra (black filled circles). Top and middle panels: 3.6 μm vs. 0.5–2 keV, 4.5 μm vs. 0.5–2 keV, 3.6 μm vs. 2–7 keV, and 4.5 μm vs. 2–7 keV. We overplot our reconstruction of known $z < 6$ populations: dashed line for AGNs, dotted–dashed line for star-forming galaxies, dotted lines for hot gas in clusters, and solid lines for the sum. Bottom panels: cross-power of combined CIB (3.6 + 4.5 μm) vs. (left) soft X-ray (0.5–2 keV) and (right) hard X-ray (2–7 keV) bands.

We detect a cross-power signal that is well explained on small scales (<20 arcsec) by unresolved, known sources (galaxies, AGNs, clusters) but on larger scales in excess at $\sim 5\sigma$ of those populations (Figure 2). Scaling up the contribution from known sources to match the large-scale cross-power from clustering would strongly overpredict the signal on small scales from shot noise.

We considered possible explanations for the observed excess cross-power on large scales. Yue et al. (2013) proposed that the observed CIB–CXB coherence could be explained by a population of Compton-thick DCBHs at $z > 12$. However, by $z \sim 10$ their model would already produce an accreted mass-density of BHs greater than the locally observed value (Helgason et al. 2016). Perhaps by tuning the parameters, their

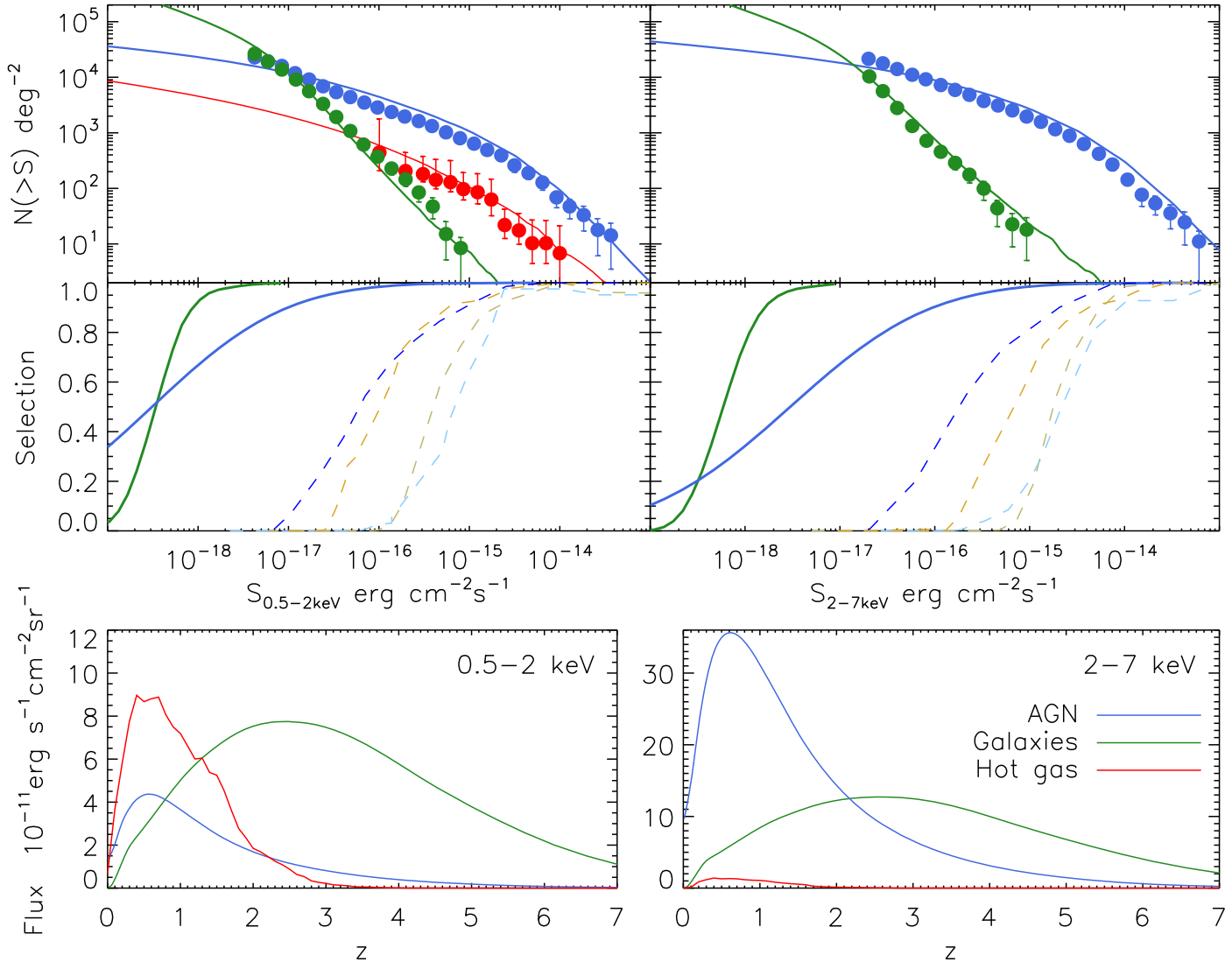

Figure 3. Top: X-ray source counts for AGNs, galaxies (Luo et al. 2017), and clusters/groups (Finoguenov et al. 2015) shown in blue, green, and red, respectively, in soft X-ray (0.5–2 keV; left) and hard X-ray (2–7 keV; right). Our models are shown as solid lines for comparison. Middle: the fraction of X-ray-detected and masked sources as a function of flux in our four fields are shown as dashed lines in the same color scheme as Figure 1. Solid lines show the modeled AGNs (blue) and galaxies (green) remaining after applying the joint X-ray/IR mask. Bottom: remaining unresolved CXB emission from cosmic populations contributing to the cross-power (same color scheme as above).

model could satisfy this integral constraint while still allowing massive rapidly growing DCBHs to account for much of the observed excess.

Kashlinsky (2016) recently proposed that primordial BHs, if they exist in sufficient numbers to account for the entire dark matter content of the universe, would produce the extra small-scale power in matter fluctuations to explain the measured *Spitzer*-based CIB fluctuations. In that case, accreting BHs like those observed with LIGO (Abbott et al. 2016), with masses ∼20–60 $M_{\odot}$, could naturally produce part or all of the observed excess.

Cooray et al. (2012a) and Zemcov et al. (2014) suggested that "orphan" stars at $z \sim 1$–5 in a diffuse intra-halo light could fully explain the detected excess CIB fluctuation. Our measurement of the CIB versus CXB coherence means that intra-halo light could produce most of the CIB excess only if a substantial fraction (larger than that observed in galaxies) of the orphan stars are X-ray binaries or pulsars or share the same environment with hot X-ray emitting gas.

Finally, some fraction of the CIB excess may arise from Galactic light scattered by interstellar dust. This diffuse Galactic light is very faint at 3.6 and 4.5 μm and is generally estimated through extrapolation from, or cross-correlation with, much brighter interstellar emission at other wavelengths (e.g., Kashlinsky 2005; Arendt et al. 2011; Matsumoto et al. 2011; Zemcov et al. 2014; Seo et al. 2015). Galactic X-rays also scatter in the diffuse ISM (Molaro et al. 2014) and thus might correlate with the IR. However, X-ray scattering is predominantly a small angle phenomenon, dropping sharply with increasing angular scale (Smith & Dwek 1998; Valencic & Smith 2015), so the X-ray sources would have to be within ∼1000″ of the survey fields. At the high latitudes of the deep surveys, there are very few Galactic sources (Lehmer et al. 2012), and we estimate the flux of such a component to ∼10 below our fluctuations.

Forthcoming missions like *Euclid, WFIRST, JWST, eROSITA*, and *Athena* offer powerful new ways to address the true nature of the cross CIB–CXB fluctuations.

N.C. thanks Yale University for the YCAA Prize Postdoctoral Fellowship. We acknowledge NASA ADAP grant NNX16AF29G, *Chandra* SAO grant AR6-17017B, *Chandra* SAO grant GO5-16150A, and NASA/12-EUCLID11-0003.

Facilities: CXO (ACIS), *Spitzer* (IRAC).

ORCID iDs

N. Cappelluti https://orcid.org/0000-0002-1697-186X
G. Hasinger https://orcid.org/0000-0002-0797-0646
K. Helgason https://orcid.org/0000-0002-4326-9144
M. Urry https://orcid.org/0000-0002-0745-9792
P. Natarajan https://orcid.org/0000-0002-5554-8896
A. Finoguenov https://orcid.org/0000-0002-4606-5403

References

Abbott, B. P., Abbott, R., Abbott, T. D., et al. 2016, PhRvL, 116, 061102
Alexander, D. M., Bauer, F. E., Brandt, W. N., et al. 2003, AJ, 126, 539
Arendt, Richard G., Kashlinsky, A., Moseley, S. H., & Mather, J. 2011, ApJS, 186, 10
Basu-Zych, A. R., Lehmer, B. D., Hornschemeier, A. E., et al. 2013, ApJ, 762, 45
Bird, S., Cholis, I., Muñoz, J. B., et al. 2016, PhRvL, 116, 201301
Cappelluti, N., Kashlinsky, A., Arendt, R. G., et al. 2013, ApJ, 769, 68
Cappelluti, N., Li, Y., Ricarte, A., et al. 2017, ApJ, 837, 19
Civano, F., Elvis, M., Brusa, M., et al. 2012, ApJS, 201, 30
Cooray, A., Gong, Y., Smidt, J., & Santos, M. G. 2012a, ApJ, 756, 92
Cooray, A., Smidt, J., de Bernardis, F., et al. 2012b, Natur, 490, 514
Erfanianfar, G., Finoguenov, A., Tanaka, M., et al. 2013, ApJ, 765, 117
Erfanianfar, G., Popesso, P., Finoguenov, A., et al. 2014, MNRAS, 445 2725
Finoguenov, A., Tanaka, M., Cooper, M., et al. 2015, A&A, 576, A130
Finoguenov, A., Watson, M. G., Tanaka, M., et al. 2010, MNRAS, 403, 2063
Gilli, R., Comastri, A., & Hasinger, G. 2007, A&A, 463, 79
Goulding, A. D., Forman, W. R., Hickox, R. C., et al. 2012, ApJS, 202, 6
Guo, Q., White, S., Boylan-Kolchin, M., et al. 2011, MNRAS, 413, 101
Helgason, K., Cappelluti, N., Hasinger, G., Kashlinsky, A., & Ricotti, M. 2014, ApJ, 785, 38
Helgason, K., Ricotti, M., & Kashlinsky, A. 2012, ApJ, 752, 113
Helgason, K., Ricotti, M., Kashlinsky, A., & Bromm, V. 2016, MNRAS, 455, 282
Henriques, B. M. B., White, S. D. M., Thomas, P. A., et al. 2015, MNRAS, 451, 2663
Hickox, R. C., & Markevitch, M. 2006, ApJ, 645, 95
Kashlinsky, A. 2005, PhR, 409, 361
Kashlinsky, A. 2016, ApJL, 823, L25
Kashlinsky, A. 2017, RvMP, submitted
Kashlinsky, A., Arendt, R. G., Ashby, M. L. N., et al. 2012, ApJ, 753, 63
Kashlinsky, A., Arendt, R. G., Mather, J., & Moseley, S. H. 2005, Natur, 438, 7064
Kashlinsky, A., Arendt, R. G., Mather, J., & Moseley, S. H. 2007a, ApJL, 654, L5
Kashlinsky, A., Arendt, R. G., Mather, J., & Moseley, S. H. 2007b, ApJL, 654, L1
Kashlinsky, A., Mather, J. C., Helgason, K., et al. 2015, ApJ, 804, 99
Kashlinsky, A., Odenwald, S., Mather, J., Skrutskie, M. F., & Cutri, R. M. 2002, ApJL, 579, L53
Kolodzig, A., Gilfanov, M., Hütsi, G., & Sunyaev, R. 2017, MNRAS, 466, 3035
Lehmer, B. D., Basu-Zych, A. R., Mineo, S., et al. 2016, ApJ, 825, 7
Lehmer, B. D., Xue, Y. Q., Brandt, W. N., et al. 2012, ApJ, 752, 46
Lodato, G., & Natarajan, P. 2006, MNRAS, 371, 1813
Lodato, G., & Natarajan, P. 2007, MNRAS, 377, L64
Luo, B., Brandt, W. N., Xue, Y. Q., et al. 2017, ApJS, 228, 2
Matsumoto, T., Seo, H. J., Jeong, W.-S., et al. 2011, ApJ, 742, 124
Mitchell-Wynne, K., Cooray, A., Xue, Y., et al. 2016, ApJ, 832, 104
Molaro, M., Khatri, R., & Sunyaev, R. A. 2014, A&A, 564, A107
Nandra, K., Laird, E. S., Aird, J. A., et al. 2015, ApJS, 220, 10
Odenwald, S., Kashlinsky, A., Mather, J. C., Skrutskie, M. F., & Cutri, R. M. 2003, ApJ, 583, 535
Seo, H. J., Lee, H. M., Matsumoto, T., et al. 2015, ApJ, 807, 140
Smith, R. K., & Dwek, E. 1998, ApJ, 503, 831
Thompson, R. I., Eisenstein, D., Fan, X., Rieke, M., & Kennicutt, R. C. 2007a, ApJ, 666, 658
Thompson, R. I., Eisenstein, D., Fan, X., Rieke, M., & Kennicutt, R. C. 2007b, ApJ, 657, 669
Valencic, L. A., & Smith, R. K. 2015, ApJ, 809, 66
Yue, B., Ferrara, A., Salvaterra, R., Xu, Y., & Chen, X. 2013, MNRAS, 433, 1556
Zemcov, M., Smidt, J., Arai, T., et al. 2014, Sci, 346, 732